Avalanche Gain in Metal−Semiconductor−Metal Ga$_2$O$_3$ Solar-Blind Photodiodes

Baoshi Qiao,[†,‡] Zhenzhong Zhang,[*,†,§] Xiuhua Xie,[†] Binghui Li,[†] Kexue Li,[†] Xing Chen,[†] Haifeng Zhao,[†] Kewei Liu,[†] Lei Liu,[†] and Dezhen Shen[*,†]

[†]State Key Laboratory of Luminescence and Applications, Changchun Institute of Optics, Fine Mechanics and Physics, Chinese Academy of Sciences, No. 3888 Dongnanhu Road, Changchun, 130033, People's Republic of China

[‡]University of the Chinese Academy of Sciences, Beijing 100049, People's Republic of China

[§]Center of Materials Science and Optoelectronics Engineering, University of Chinese Academy of Sciences, Beijing 100049, China

ABSTRACT: Metal−semiconductor−metal structured photodetectors based on *β*-Ga$_2$O$_3$ thin films were fabricated. Because of the high dark-resistance and considerable photoconduction, extremely uneven distribution of electric field is formed in the device under solar-blind UV light-illumination when a bias is added. Avalanche multiplication takes place in the high-field area near the electrode edges. Responsivity up to 46 A/W and the corresponding external quantum efficiency of 23 000% are observed. The photodetector shows a peak response at 248 nm, a sharp cut off edge at 262 nm (at −20 dB), and a fast response speed with a fall time of about 26.7 *μ*s. Because of the ultralow response out of band, the rejection ratio $R_{254/365nm}$ is larger than 7 orders of magnitude, where the illumination intensity at 254 and 365 nm are 0.5 and 1.2 mW/cm^2, respectively.
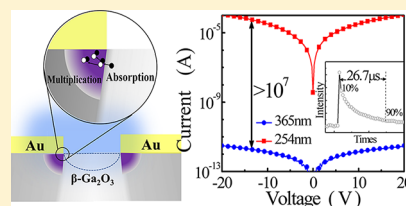
1. INTRODUCTION

Avoiding interference from sunlight, solar-blind photodiodes have broad applications in many fields,[1,2] such as space communication, air/water pollutant detection, missile early warning, and so forth.[3−5] In these applications, the detection ability to ultraweak light signal becomes more and more necessary. For instance, the flame luminescence detection requires a sensitivity of 1 nW/cm^2.[6] Excellent rejection ratio (or response selectivity) and photo/dark current ratio are the bases of weak light detection performance. Wide-band-gap semiconductors such as AlGaN, MgZnO, diamond, and Ga$_2$O$_3$ are considered as the ideal materials for solar-blind UV detection because their band gaps endow them with intrinsic response selectivity.[7−9] Lots of efforts have been made to increase further the detection ability by improving material quality and device design.[10−12] For instance, graphene was used as a transparent electrode in place of a metal to improve responsivity and rejection ratio, because the metal electrodes usually shelter partly the incidence light and the high-resistant area left under the electrodes decreases the photocurrent in most photodetectors.[13,14] However, in fact, a higher rejection ratio and photo/dark current ratio can be obtained in a simple metal−semiconductor−metal (MSM) device.[15] There may be other gain besides photoconductive gain in the device, although it was scarcely discussed in previous reports.

In this work, we fabricated MSM structured Ga$_2$O$_3$ solar-blind UV photodiodes with ultralow dark current. The large responsivity increasing with illumination intensity and rapid response speed indicate avalanche gain in this device. The high-resistant areas under electrodes play the multiplication region due to extremely uneven distribution of electric field in the photodiode. Thanks for the avalanche gain existing in the

MSM device, the device shows an excellent rejection ratio at 254/365 nm.

2. EXPERIMENTAL SECTION

The *β*-Ga$_2$O$_3$ thin films were grown on *c*-plane sapphire by metal-organic chemical vapor deposition (MOCVD). After ultrasonic bathing in trichloro ethylene, acetone, ethyl alcohol, and deionized water, the substrate was put into a growth chamber. The growth temperature was kept at 650 °C. The chamber pressure was held at 500 Pa. Triethylgallium and 5 N O$_2$ were used as the precursors with flow rates of 0.22 mmol/min and 60 SCCM (standard-state cubic centimeter per minute), respectively. The carrier gas was 6 N nitrogen evaporated from liquid nitrogen. The thermal annealing was carried out in air atmosphere for 20 min. The annealing temperatures were 600, 700, 800, and 900 °C. The MSM-structured device with interdigital electrodes was fabricated by sputtering gold and the following lithography. The lithography was carried out on a H94-25C (Sichuan Nanguang Vacuum Tech. Co. Ltd.) contact aligner. After covering the wafer with a negative photoresist (KMP E3130A), the sample was prebaked at 90 °C for 3 min and exposed for 5 s. The postexposure bake was performed at 90 °C for 3 min. Then, the sample was developed in the stripper (SP-01) for 10 s. A 100 nm-thick Au thin film was deposited on the thin film, followed by 3 min ultrasonic bathing to remove any residual Au. The effective working area of the device contains 25 pairs of fingers, covering

an area of 0.5×1 mm^2. Both the width of single Au finger and the interval between fingers are 10 μm.

The morphology and structure of β-Ga$_2$O$_3$ films were characterized by scanning electron microscopy (SEM) (Hitachi S-4800) and X-ray diffraction (XRD) (Bruker D8GADDS) with Cu Kα radiation (λ = 0.154 nm). The transmittance spectra were measured on a Shimadzu UV-3101PC Spectrophotometer. The $I-V$ characteristics were measured on a semiconductor device analyzer (Agilent B1500A). The photoresponse was measured using a responsivity measurement system equipped with an SR 830 lock-in amplifier and a 150 W Xe lamp. The time resolution response was recorded by a Tektronix DPO5104 oscilloscope using a pulsed Nd:YAG laser at the 266 nm with 10 ns pulse width as the excitation source.

3. RESULTS AND DISCUSSION

The SEM photographs of the as-grown and 800 °C-annealed Ga$_2$O$_3$ thin films are shown in the Figure 1a,b. Compared to
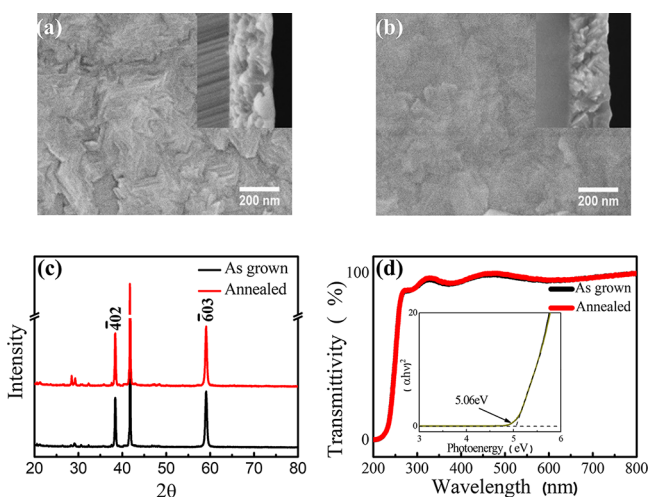

Figure 1. SEM images of the as-grown (a) and 800 °C thermal-annealed (b) β-Ga$_2$O$_3$ thin films. The associated cross-sectional images are shown in the insets. (c) XRD patterns of as-grown and 800 °C-annealed β-Ga$_2$O$_3$ thin films. (d) Optical transmittance spectra of the β-Ga$_2$O$_3$ films. The inset shows the band-gap fit of the β-Ga$_2$O$_3$ film.

the as-grown thin film, the surface of the annealed sample looks smoother, indicating that the grains fuse each other. It decreases the specific surface area in a certain degree, thus

decreasing the surface state density. The thickness of the film is about 220 nm, as shown in the cross-profile image in the insets. The XRD spectra are exhibited in Figure 1c. It can be found that the as-grown sample is crystallized in single β phase with the preferred (−201) orientation. After annealing, the full width at half-maximum (fwhm) of (−402) peak decreases from 0.262° to 0.245°. It indicates that the grains grew up during the annealing process, meaning the decrease of grain boundary. The transmittance spectra of the β-Ga$_2$O$_3$ thin films are shown in Figure 1d. The sample shows a sharp absorption edge and has almost no change in transmittance characteristic after annealing. The gap energy (E_g) calculated by the Tauc law for the direct-band-gap semiconductor is 5.06 eV, as shown in the inset, which is consistent with most reported values.[16] The sharp absorption edge and the transmission efficiency higher than 92% for the photon with wavelengths larger than 300 nm reflect the satisfying crystal quality of the Ga$_2$O$_3$ thin films.

To investigate the influence of annealing on electrical properties, interdigital gold electrodes were fabricated on the β-Ga$_2$O$_3$ thin films by sputtering and lithography. Naturally, an MSM-structured photodetector was obtained. Both the finger width and finger spacing are 10 μm. Figure 2a shows the evolvement of dark current and photocurrent at 20 V bias with increasing annealing temperature. A 254 nm line of mercury lamp was used as the light source and the illumination intensity is 0.5 mW/cm^2. With the increase of annealing temperature, the photocurrent increases first and drops afterward. At 800 °C, the photocurrent reaches its maximum of 115 μA. After annealing at 900 °C, the photocurrent drops abruptly. In contrast, the dark current shows a monotonic and marked decrease by about 10^3 with increasing annealing temperature. At 800 °C, the dark current is as low as hundreds of femtoampere, as shown in the inset. To investigate the origin of this drastic change in conductivity, electric characterization was performed on a Hall measurement system HMS7707 (Lakeshore Inc.). Considering that the ultrahigh resistivity of undoped β-Ga$_2$O$_3$ beyond the measurement range of HMS 7707, a 254 nm illumination from a mercury lamp was used to decrease the resistance so that the Hall characterization can be performed. In this case, the measurement cannot provide the real carrier density but can reflect the carrier mobility roughly. The measured Hall mobility values of as-grown and 800 °C-annealed Ga$_2$O$_3$ thin films were 3.5 and 1.9 cm^2/V s, respectively. Such values close to each other indicate that the change of mobility after annealing is not the major reason for the great change in resistivity. In other words, the change of dark current can only be dominated by a sharp decrease of
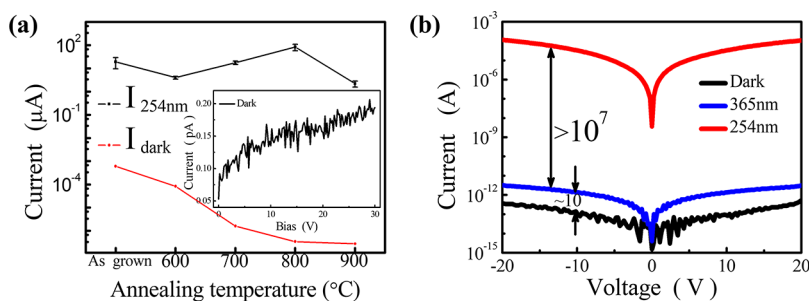

Figure 2. (a) Light and dark currents at 20 V bias after annealing at different temperatures. The inset shows the dark current of 800 °C-annealed β-Ga$_2$O$_3$ thin film in linear coordinates. (b) $I-V$ characteristics of the 800 °C-annealed β-Ga$_2$O$_3$ thin film in dark, under 254 nm (0.5 mW/cm^2) and 365 nm (1.2 mW/cm^2) illuminations, respectively.

carrier concentration, which may benefit from the repairing of donorlike defects during thermal annealing.[12] As seen, the device shows the largest light/dark current ratio after 800 °C annealing. In the following, all the "annealed" samples refer to the 800 °C annealed ones.

Figure 2b shows the $I-V$ curves for the annealed sample under 254 nm illumination and 365 nm illumination and in dark. The photo/dark current ratio is calculated to be larger than 10^8. The detection selectivity is a key parameter for solar-blind photodetection, which is usually depicted by the rejection ratio. Under the 365 nm illumination with power intensity of 1.2 mW/cm^2, the photocurrent at bias of 20 V is only 3.1 pA. According to the photocurrent ratio at 254/365 nm, the calculated rejection ratio is up to 3.7×10^7.

Responsivity is often used to evaluate the detection ability. It can be calculated by the following formula:[17,18]

$$R_\lambda = (I_\lambda - I_d)/P_\lambda S \tag{1}$$

where I_λ is the photocurrent, P_λ is the intensity of the illumination at wavelength λ, I_d is the dark current, and S is the effective area.[19] Here, the effective illuminated area is 500×1000 μm^2. Under the 254 nm illumination with intensity of 0.5 mW/cm^2, the responsivity is calculated to be 46 A/W at 20 V.

Detectivity is another performance index to evaluate the detection sensitivity. It can be calculated by[20,21]

$$D^* = R/\sqrt{2qJ_d} \tag{2}$$

where R is the peak responsivity, q is the elemental charge, and J_d is the density of the dark current which is 68.6 pA/cm^2 in this work. Because of the ultralow dark current density, the detectivity reaches 9.8×10^{15} cm Hz$^{1/2}$/W at 20 V.

According to the responsivity, we can obtain the external quantum efficiency (EQE) through[22,23]

$$\eta = R_\lambda h\nu/q \tag{3}$$

where R_λ is the responsivity, $h\nu$ is the energy of incident photon, and q is the elemental charge. The peak EQE is about 23 000%. It indicates considerable gain existing in the device. The inset of Figure 3b shows the $I-V$ curve under 254 nm illumination with 22 nW/cm^2. A rapid increase of photocurrent is observed when the bias exceeds 5 V. It suggests that a gain with threshold takes place in the device. The gain mechanism is considered to contain the avalanche process, as shown in the Figure 3a. Under the illumination of 254 nm UV light, most of the electric field is localized in the high-resistant areas beneath the electrodes due to the photoconduction, as the band diagram depicted. The photogenerated electron and hole are separated and swapped into the high field area beneath electrodes. Here, the carriers are accelerated greatly and impact the lattice. The impact ionization triggers the avalanche multiplication process.[24] Figure 3b shows the $I-V$ curves under 254 nm illumination with different intensities. Every curve shows a rapid increase after the bias beyond a certain value. With the illumination intensity increasing from 2 to 82.2 nW/cm^2, the inflection voltage decreases from 11.7 to 2.4 V gradually. This shift evolvement of the inflection is shown in Figure 3c, which supports well the avalanche multiplication proposed above. The higher the illumination intensity is, the more uneven the resistance distributes. Thus, the added field concentrates more and more in the area beneath electrode by increasing the illumination level. This suggests that the avalanche threshold voltage decreases
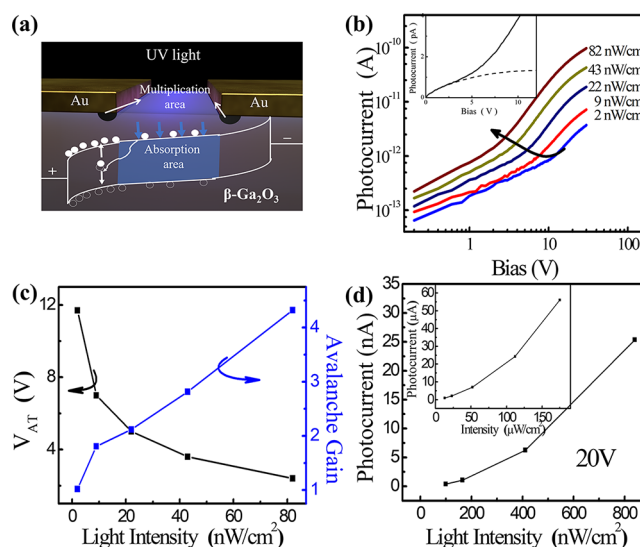

Figure 3. (a) Diagram and band diagram of the electric field-distribution in the high-resistant area under the electrodes. (b) Photocurrent at different illumination intensities. The inset shows the band diagram under illumination (c) Change of the avalanche threshold voltage at different illumination intensities. The blue line shows the avalanche gain at different illumination intensities. (d) Photocurrent changes with increasing illumination intensity. The inset shows the photocurrent change at higher illumination intensity. All the bias voltages are 20 V.

gradually. Correspondingly, because the electric field near electrode becomes stronger at a higher illumination level, the impact ionization gain will be larger at the same added bias. The expected change of gain is observed, as shown by the blue curve in Figure 3c, where the avalanche gain is calculated by the photocurrent and dark current before/after avalanche. Figure 3d shows the photocurrents biased at 20 V under various illumination intensities. The photocurrent keeps a superlinear increasing tendency in a large illumination intensity range. Such a superlinear increase of photocurrent with illumination is distinct with the saturation behavior in the device containing only traditional avalanche gain or photoconduction gain.[25]

The photoresponse spectra are shown in Figure 4a. To evaluate the performance of the device clearly, the responsivity is drawn in log coordinates. The response peaks at 248 nm and sharply cuts-off (−20 dB) at 262 nm. The rejection ratio at peak/280 nm is over 3 orders of magnitude. Almost no response can be observed for the wavelength longer than 330 nm, indicating a good solar-blind characteristic. Note that the $R_{254/365nm}$ rejection ratio is calculated to be 3.5×10^6, which is smaller by about 1 order of magnitude than the calculated value according to the $I-V$ curves in Figure 2b. This is because the responsivity minimum is limited by the background noise of the lock-in amplifier and the smaller responsivity at lower illumination (0.04 mW/cm^2) than that at high illumination (0.5 mW/cm^2). Figure 4b shows the time response under pulse laser excitation. The decay time from 90 to 10% of maximum is 26.7 μs, containing a fast process with $\tau_1 = 0.9$ μs and a slower process with $\tau_2 = 11.9$ μs. This response speed is superior to the fastest Ga$_2$O$_3$ photodetectors reported previously.[25,26] The responsivity as large as 46 A/W and the fast response distinct with common MSM photodiodes further support that the response is dominated mainly by avalanche
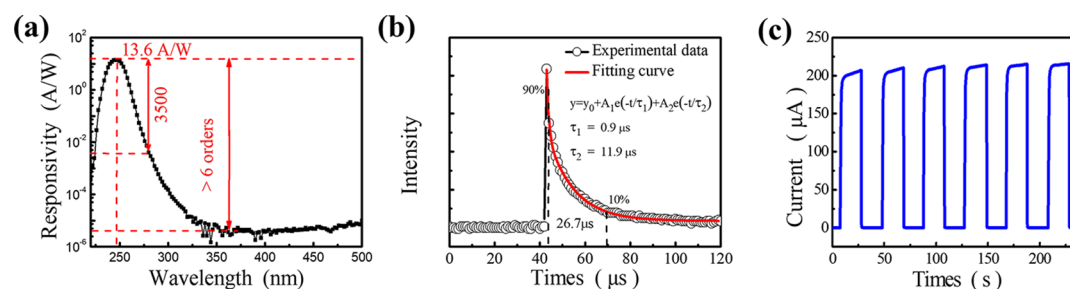
Figure 4. (a) Photoresponse spectrum in a log coordinate, where the bias is 30 V. (b) Time response under the excitation of 266 nm pulsed laser (tune to 250 nm). (c) Time response characteristics of the "on" and "off" states under the 254 nm illumination with 0.5 mW/cm^2 at 30 V.

Table 1. Characteristics of the Annealed β-Ga$_2$O$_3$ Photodetector and Other Solar-Blind UV Photodetectors in the Literature Studies

photodetector	rejection ratio	responsivity [A/W] (voltage)	detectivity (cm Hz$^{1/2}$/W)	decay time [μs] T$_1$	T$_2$	refs
Au/Ga$_2$O$_3$	10^6 (240 nm/350 nm)	1000 (3 V)				10
ZnO/Ga$_2$O$_3$ core–shell microwire	5 × 10^3 (254 nm/400 nm)	1300 (6 V)	9.91 × 10^{14}	42	815	11
Au/β-Ga$_2$O$_3$	2 × 10^3 (258 nm/400 nm)	0.0029 (50 V)		64		25
α-Ga$_2$O$_3$ MSM	>10^4 (light/dark)	0.19 (20 V)		19.1	80.7	26
MgZnO MSM	10^4 (290 nm/400 nm)	0.0105 (5 V)		0.03		27
α-Ga$_2$O$_3$/ZnO	10^3 (230 nm/450 nm)	0.00342 (0 V)	9.66 × 10^{12}	238	3.04 × 10^3	28
AlGaN MSM	10^6 (250 nm/400 nm)	1 000 000 (5 V)				29
Zn$_2$GeO$_4$ NW	~10 (light/dark)	5110 (1 V)	2.91 × 10^{11}	1.3 × 10^4		30
β-Ga$_2$O$_3$ MSM	10^5 (236 nm/420 nm)	1.5 (4 V)		4 × 10^5		31
β-Ga$_2$O$_3$ MSM	2 × 10^4 (236 nm/320 nm)	46 (20 V)		800		32
β-Ga$_2$O$_3$ MSM	10^7 (254 nm/365 nm)	46 (20 V)	9.8 × 10^{15}	0.9	11.9	this work

gain rather than the photoconduction one. The device also possesses good stability and repeatability, as shown in Figure 4c, where the illumination wavelength is 254 nm and the bias is 30 V.

Table 1 lists the important performance indexes of reported SBPDs based on wide-band-gap materials and this device, including rejection ratio, responsivity, and response speed.[33] The device in this work shows the highest rejection ratio among these photodetectors. Moreover, as an MSM-structured device, the response speed is also at a relative high level in these reports.[34]

4. CONCLUSIONS

In summary, we realized a MSM-structured solar-blind photodiode with avalanche gain based on Ga$_2$O$_3$ thin film and explained the relationship between the avalanche gain and rejection ratio. The extremely unbalanced distribution of electric field caused by electrode sheltering and photoconduction is considered as the key premise for the avalanche gain. The device shows a rejection ratio at 254/365 nm larger than 10^7, a peak responsivity of 46 A/W at 20 V bias, and a high response speed with a fall time of 26.7 μs. This work provides a simple route to realize solar-blind photodiodes with high spectral selectivity, which can be used in ultraweak solar-blind UV detection.

■ AUTHOR INFORMATION

Corresponding Authors
*E-mail: zhangzz@ciomp.ac.cn (Z.Z.).
*E-mail: shendz@ciomp.ac.cn (D.S.).

ORCID
Baoshi Qiao: 0000-0002-5095-1344
Lei Liu: 0000-0002-9714-2130

Author Contributions

The manuscript was written through contributions of all authors. All authors have given approval to the final version of the manuscript.

Notes

The authors declare no competing financial interest.

■ ACKNOWLEDGMENTS

■ ABBREVIATIONS

UV, ultraviolet; MSM, metal−semiconductor−metal; MOCVD, metal-organic chemical vapor deposition; SCCM, standard-state cubic centimeter per minute; SEM, scanning electron microscopy; XRD, X-ray diffraction; fwhm, full width at half-maximum; EQE, external quantum efficiency

■ REFERENCES

(1) Chen, H.; Yu, P.; Zhang, Z.; Teng, F.; Zheng, L.; Hu, K.; Fang, X. Ultrasensitive Self-Powered Solar-Blind Deep-Ultraviolet Photo-

detector Based on All-Solid-State Polyaniline/MgZnO Bilayer. *Small* **2016**, *12*, 5809−5816.

(2) Lee, S. H.; Kim, S. B.; Moon, Y.-J.; Kim, S. M.; Jung, H. J.; Seo, M. S.; Lee, K. M.; Kim, S.-K.; Lee, S. W. High-Responsivity Deep-Ultraviolet-Selective Photodetectors Using Ultrathin Gallium Oxide Films. *ACS Photonics* **2017**, *4*, 2937−2943.

(3) Cui, W.; Guo, D.; Zhao, X.; Wu, Z.; Li, P.; Li, L.; Cui, C.; Tang, W. Solar-Blind Photodetector Based on Ga_2O_3 Nanowires Array Film Growth from Inserted Al_2O_3 Ultrathin Interlayers for Improving Responsivity. *RSC Adv.* **2016**, *6*, 100683−100689.

(4) An, Y.; Chu, X.; Huang, Y.; Zhi, Y.; Guo, D.; Li, P.; Wu, Z.; Tang, W. Au Plasmon Enhanced High Performance β-Ga_2O_3 Solar-Blind Photo-Detector. *Prog. Nat. Sci.: Mater. Int.* **2016**, *26*, 65−68.

(5) Syed, N.; Zavabeti, A.; Mohiuddin, M.; Zhang, B.; Wang, Y.; Datta, R. S.; Atkin, P.; Carey, B. J.; Tan, C.; van Embden, J.; et al. Sonication-Assisted Synthesis of Gallium Oxide Suspensions Featuring Trap State Absorption: Test of Photochemistry. *Adv. Funct. Mater.* **2017**, *27*, 1702295.

(6) Oshima, T.; Okuno, T.; Arai, N.; Suzuki, N.; Hino, H.; Fujita, S. Flame Detection by a β-Ga_2O_3-Based Sensor. *Jpn. J. Appl. Phys.* **2009**, *48*, 011605.

(7) Xie, F.; Lu, H.; Chen, D.; Ji, X.; Yan, F.; Zhang, R.; Zheng, Y.; Li, L.; Zhou, J. Ultra-Low Dark Current AlGaN-Based Solar-Blind Metal-Semiconductor-Metal Photodetectors for High-Temperature Applications. *IEEE Sens. J.* **2012**, *12*, 2086−2090.

(8) Hwang, J. D.; Lin, G. S. Single- and Dual-Wavelength Photodetectors with MgZnO/ZnO Metal-Semiconductor-Metal Structure by Varying the Bias Voltage. *Nanotechnology* **2016**, *27*, 375502.

(9) Chen, Y.-C.; Lu, Y.-J.; Lin, C.-N.; Tian, Y.-Z.; Gao, C.-J.; Dong, L.; Shan, C.-X. Self-Powered Diamond/β-Ga_2O_3 Photodetectors for Solar-Blind Imaging. *J. Mater. Chem. C* **2018**, *6*, 5727−5732.

(10) Suzuki, R.; Nakagomi, S.; Kokubun, Y.; Arai, N.; Ohira, S. Enhancement of Responsivity in Solar-Blind β-Ga_2O_3 Photodiodes with a Au Schottky Contact Fabricated on Single Crystal Substrates by Annealing. *Appl. Phys. Lett.* **2009**, *94*, 222102.

(11) Zhao, B.; Wang, F.; Chen, H.; Wang, Y.; Jiang, M.; Fang, X.; Zhao, D. Solar-Blind Avalanche Photodetector Based on Single ZnO-Ga_2O_3 Core-Shell Microwire. *Nano Lett.* **2015**, *15*, 3988−3993.

(12) Rafique, S.; Han, L.; Zhao, H. Thermal Annealing Effect on β-Ga_2O_3 Thin Film Solar Blind Photodetector Heteroepitaxially Grown on Sapphire Bubstrate. *Phys. Status Solidi A* **2017**, *214*, 1700063.

(13) Kong, W.-Y.; Wu, G.-A.; Wang, K.-Y.; Zhang, T.-F.; Zou, Y.-F.; Wang, D.-D.; Luo, L.-B. Graphene-β-Ga_2O_3 Heterojunction for Highly Sensitive Deep UV Photodetector Application. *Adv. Mater.* **2016**, *28*, 10725−10731.

(14) Oh, S.; Kim, C.-K.; Kim, J. High Responsivity β-Ga_2O_3 Metal−Semiconductor−Metal Solar-Blind Photodetectors with Ultraviolet Transparent Graphene Electrodes. *ACS Photonics* **2017**, *5*, 1123−1128.

(15) Tsai, S.-H.; Basu, S.; Huang, C.-Y.; Hsu, L.-C.; Lin, Y.-G.; Horng, R.-H. Deep-Ultraviolet Photodetectors Based on Epitaxial $ZnGa_2O_4$ Thin Films. *Sci. Rep.* **2018**, *8*, 14056.

(16) Zhuo, Y.; Chen, Z.; Tu, W.; Ma, X.; Pei, Y.; Wang, G. β-Ga_2O_3 versus ε-Ga_2O_3: Control of the Crystal Phase Composition of Gallium Oxide Thin Film Prepared by Metal-Organic Chemical Vapor Deposition. *Appl. Surf. Sci.* **2017**, *420*, 802−807.

(17) Hatch, S. M.; Briscoe, J.; Dunn, S. A Self-Powered ZnO-Nanorod/CuSCN UV Photodetector Exhibiting Rapid Response. *Adv. Mater.* **2013**, *25*, 867−871.

(18) Ding, J.; Du, S.; Zuo, Z.; Zhao, Y.; Cui, H.; Zhan, X. High Detectivity and Rapid Response in Perovskite $CsPbBr_3$ Single-Crystal Photodetector. *J. Phys. Chem. C* **2017**, *121*, 4917−4923.

(19) Weng, W. Y.; Hsueh, T. J.; Chang, S. J.; Huang, G. J.; Hsueh, H. T. A β-Ga_2O_3 Solar-Blind Photodetector Prepared by Furnace Oxidization of GaN Thin Film. *IEEE Sens. J.* **2011**, *11*, 999−1003.

(20) Bo, R.; Nasiri, N.; Chen, H.; Caputo, D.; Fu, L.; Tricoli, A. Low-Voltage High-Performance UV Photodetectors: An Interplay between Grain Boundaries and Debye Length. *ACS Appl. Mater. Interfaces* **2017**, *9*, 2606−2615.

(21) Luo, X.; Chen, S.; Liu, L.; Lv, J.; Qadir, A.; Shehzad, K.; Qiao, X.; Xu, Y.; Kienle, L.; Lotnyk, A.; et al. Micron-Scale Photodetectors Based on One-Dimensional Single-Crystalline $Sb_{2-x}Sn_xSe_3$ Microrods: Simultaneously Improving Responsivity and Extending Spectral Response Region. *J. Phys. Chem. C* **2018**, *123*, 810−816.

(22) Shin, S. W.; Lee, K.-H.; Park, J.-S.; Kang, S. J. Highly Transparent, Visible-Light Photodetector Based on Oxide Semiconductors and Quantum Dots. *ACS Appl. Mater. Interfaces* **2015**, *7*, 19666−19671.

(23) Zhang, D.; Xu, R.; Sun, L.; Chen, C.; Gao, F.; Zhang, X.; Zhou, J.; Ruan, S. Mechanism of Polyfluorene Interlayer in Ultraviolet Photodetector: Barrier-Blocking Electron Transport and Light-Inducing Hole Injection. *J. Phys. Chem. C* **2016**, *120*, 26103−26109.

(24) Hu, G. C.; Shan, C. X.; Zhang, N.; Jiang, M. M.; Wang, S. P.; Shen, D. Z. High Gain Ga_2O_3 Solar-Blind Photodetectors Realized Via a Carrier Multiplication Process. *Opt. Express* **2015**, *23*, 13554−13561.

(25) Chen, R. S.; Chen, C. A.; Tsai, H. Y.; Wang, W. C.; Huang, Y. S. Photoconduction Properties in Single-Crystalline Titanium Dioxide Nanorods with Ultrahigh Normalized Gain. *J. Phys. Chem. C* **2012**, *116*, 4267−4272.

(26) Chen, X.; Liu, K.; Zhang, Z.; Wang, C.; Li, B.; Zhao, H.; Zhao, D.; Shen, D. Self-Powered Solar-Blind Photodetector with Fast Response Based on Au/β-Ga_2O_3 Nanowires Array Film Schottky Junction. *ACS Appl. Mater. Interfaces* **2016**, *8*, 4185−4191.

(27) Cui, S.; Mei, Z.; Zhang, Y.; Liang, H.; Du, X. Room-Temperature Fabricated Amorphous Ga_2O_3 High-Response-Speed Solar-Blind Photodetector on Rigid and Flexible Substrates. *Adv. Opt. Mater.* **2017**, *5*, 1700454.

(28) Zhao, Y.; Zhang, J.; Jiang, D.; Shan, C.; Zhang, Z.; Yao, B.; Zhao, D.; Shen, D. Ultraviolet Photodetector Based on a MgZnO Film Grown by Radio-Frequency Magnetron Sputtering. *ACS Appl. Mater. Interfaces* **2009**, *1*, 2428−2430.

(29) Chen, X.; Xu, Y.; Zhou, D.; Yang, S.; Ren, F.-f.; Lu, H.; Tang, K.; Gu, S.; Zhang, R.; Zheng, Y.; et al. Solar-Blind Photodetector with High Avalanche Gains and Bias-Tunable Detecting Functionality Based on Metastable Phase α-Ga_2O_3/ZnO Isotype Heterostructures. *ACS Appl. Mater. Interfaces* **2017**, *9*, 36997−37005.

(30) Yoshikawa, A.; Ushida, S.; Nagase, K.; Iwaya, M.; Takeuchi, T.; Kamiyama, S.; Akasaki, I. High-Performance Solar-Blind $Al_{0.6}Ga_{0.4}N$/$Al_{0.5}Ga_{0.5}N$ MSM Type Photodetector. *Appl. Phys. Lett.* **2017**, *111*, 191103.

(31) Zhou, X.; Zhang, Q.; Gan, L.; Li, X.; Li, H.; Zhang, Y.; Golberg, D.; Zhai, T. High-Performance Solar-Blind Deep Ultraviolet Photodetector Based on Individual Single-Crystalline Zn_2GeO_4 Nanowire. *Adv. Funct. Mater.* **2016**, *26*, 704−712.

(32) Pratiyush, A. S.; Krishnamoorthy, S.; Vishnu Solanke, S.; Xia, Z.; Muralidharan, R.; Rajan, S.; Nath, D. N. High Responsivity in Molecular Beam Epitaxy Grown β-Ga_2O_3 Metal Semiconductor Metal Solar Blind Deep-UV Photodetector. *Appl. Phys. Lett.* **2017**, *110*, 221107.

(33) Alema, F.; Hertog, B.; Ledyaev, O.; Volovik, D.; Thoma, G.; Miller, R.; Osinsky, A.; Mukhopadhyay, P.; Bakhshi, S.; Ali, H.; et al. Solar Blind Photodetector Based on Epitaxial Zinc Doped Ga_2O_3 Thin Film. *Phys. Status Solidi A* **2017**, *214*, 1600688.

(34) Oh, S.; Kim, J.; Ren, F.; Pearton, S. J.; Kim, J. Quasi-Two-Dimensional β-Gallium Oxide Solar-Blind Photodetectors with Ultrahigh Responsivity. *J. Mater. Chem. C* **2016**, *4*, 9245−9250.